Materials & Design 262 (2026) 115454

Contents lists available at ScienceDirect

Materials & Design

journal homepage: www.elsevier.com/locate/matdes

Tailored interfacial design via in situ polymer integration enhances thermoelectric performance in Bi_2Te_3

Cham Kim [a,*], Changwoo Lee [b], Hyun-Sik Kim [b], David Humberto Lopez [c]

[a] Division of Nanotechnology, Daegu Gyeongbuk Institute of Science and Technology, 333 Techno Jungang-daero, Daegu 42988, the Republic of Korea
[b] Department of Materials Science and Engineering, University of Seoul, 163 Seoulsiripdae-ro, Dongdaemun-gu, Seoul 02504, the Republic of Korea
[c] Department of Chemical and Environmental Engineering, University of Arizona, 1133 E. James. E. Rogers Way, Tucson, AZ 85721, USA

ARTICLE INFO

Keywords:
Thermoelectric materials
Spark plasma sintering
Interfaces
Electrical properties
Thermal conductivity

ABSTRACT

This study introduces a distinct interfacial engineering strategy based on in situ polymer integration, which provides an effective and controllable route for modulating charge and heat transport for the development of a high–performance thermoelectric material. A thermoelectric composite was fabricated via a reproducible one–pot chemical process, in which the conductive polymer was polymerized and simultaneously deposited onto Bi_2Te_3. This approach yielded finely dispersed polymer domains with minimized agglomeration, resulting in increased interfacial contact with Bi_2Te_3. These interfacial contacts promoted energy filtering, inducing energy–dependent carrier scattering and a clear decoupling between electrical resistivity and Seebeck coefficient. The composite also exhibited suppressed thermal conductivity, attributed to enhanced phonon and carrier scattering at the interfacial contacts. These transport behaviors were confirmed by systematic experimental characterization together with complementary theoretical modeling based on the single parabolic band approximation. The composite achieved a maximum *ZT* of ~ 1.31 at 477 K and an average *ZT* of ~ 1.15 over the temperature range of 300–550 K. In comparison to other low–temperature n–type thermoelectric materials, the composite offers not only excellent thermoelectric performance but also advantages in cost, processability, and flexible device compatibility, making it highly suitable for practical and scalable thermoelectric applications.

1. Introduction

Thermoelectric technology enables the direct conversion between thermal and electrical energy, offering promising solutions for sustainable waste heat recovery and solid–state refrigeration without the use of refrigerants [1–3]. Despite its potential to revolutionize a wide range of industries, its relatively low energy conversion efficiency remains a major limitation. To enable widespread industrial application of thermoelectric technology, enhancing the performance of thermoelectric materials to improve energy conversion efficiency is a fundamental challenge. The performance of thermoelectric materials is typically evaluated using the dimensionless figure of merit, $ZT = \alpha^2 T/(\rho\kappa)$, where α is the Seebeck coefficient, ρ is the electrical resistivity, and κ is the thermal conductivity [4–7]. Accordingly, improving thermoelectric performance can be achieved by increasing α, reducing ρ, or decreasing κ.

In recent years, significant progress in thermoelectric materials has been achieved through various strategies, which contributed to enhanced electrical properties and suppressed thermal conductivity [1–7]. These advances have markedly improved *ZT* values of many thermoelectric materials and expanded their applicability from conventional power generation to emerging areas such as wearable and microscale energy harvesting devices. For low–temperature thermoelectric applications (typically below 573 K), Bi_2Te_3–based materials have particularly benefited owing to their tunable electronic structure, diverse microstructural engineering possibilities, and compatibility with scalable processing routes. Owing to the nature of thermoelectric technology, both p–type and n–type materials are required; however, n–type Bi_2Te_3 generally exhibits inferior thermoelectric performance compared to its p–type counterpart. Numerous studies have been conducted to enhance the thermoelectric performance of n–type Bi_2Te_3, focusing on approaches such as doping various metallic or nonmetallic elements into the Bi_2Te_3 lattice [8–10], introducing different types of nanoinclusions into the Bi_2Te_3 matrix [11,12], or fabricating Bi_2Te_3–based nanostructures with dimensionalities ranging from 0D to 3D [13,14]. These efforts have improved the thermoelectric performance of n–type Bi_2Te_3

---

* Corresponding author.
E-mail address: charming0207@dgist.ac.kr (C. Kim).

https://doi.org/10.1016/j.matdes.2026.115454
Received 28 October 2025; Received in revised form 15 December 2025; Accepted 5 January 2026

through the control of charge carrier transport and phonon scattering by defect engineering, texturing, and nanostructuring, which increase electrical properties such as the power factor (α^2/ρ) and suppress thermal conductivity. In addition to Bi_2Te_3–based systems, other high–performance low–temperature thermoelectric materials (e.g., Ag_2Se [15], GeTe [16], and Mg_3Sb_2 [17]) have also been reported. Nevertheless, Bi_2Te_3 remains the most commercially relevant material in this temperature range owing to its stable performance near room temperature, mature processing technologies, and widespread device–level implementation.

Energy filtering has been widely recognized as an effective strategy to enhance the electrical properties of thermoelectric materials. Numerous studies have reported that introducing various inorganic additives (e.g., metals, semiconductors) into thermoelectric host materials can induce energy filtering effects at the interfaces between the host and additive phases [18–20]. Specifically, when additives possessing a work function comparable to that of the host material are introduced, an interfacial energy barrier can form, resulting in energy filtering. A suitably sized energy barrier selectively allows high–energy charge carriers to pass while blocking low–energy carriers, thereby enabling high–energy carriers to transport more heat and increasing the Seebeck coefficient without significantly affecting the electrical resistivity. This approach effectively decouples the interdependent relationship between these two parameters and improves the power factor. As mentioned earlier, n–type Bi_2Te_3 typically exhibits lower thermoelectric performance than its p–type counterpart, primarily due to its intrinsically smaller Seebeck coefficient, which arises from differences in the electronic density of states near the Fermi level between n–type and p–type Bi_2Te_3. Considering the smaller Seebeck coefficient, inducing an energy filtering effect is a particularly promising strategy to enhance the thermoelectric performance of n–type Bi_2Te_3 to a level comparable to that of p–type counterpart. Several research groups have demonstrated that introducing various inorganic additives (e.g., Ag, Bi_2S_3, Bi_2Se_3, and Ga_2Te_3) into n–type Bi_2Te_3–based materials can form interfacial energy barriers that induce energy filtering effects, thereby significantly improving their thermoelectric performance [21–24]. Our research group has previously demonstrated that energy filtering can also be achieved by adding cost–effective organic materials with semimetallic or semiconducting properties (namely, conductive polymers) instead of inorganic additives, particularly to n–type Bi_2Te_3 thermoelectric materials developed for low–temperature applications [25–27]. The work function of n–type Bi_2Te_3–based materials is not a single value but is known to be influenced by several factors, such as crystal structure and surface orientation, typically falling in the range of 5.1–5.3 eV [28,29]. In our previous study, we introduced a conductive polymer, PEDOT:PSS, with a slightly higher work function than that of n–type Bi_2Te_3 to form interfacial energy barriers at their interface. These energy barriers were appropriately sized to induce an energy filtering effect, significantly contributing to an enhancement in the Seebeck coefficient. In addition to its role in the energy filtering effect for thermoelectric enhancement, PEDOT:PSS is widely utilized in flexible electronics and has recently been investigated for flexible thermoelectric device development [30–32]. These growing research efforts further underscore the broad applicability of PEDOT:PSS and highlight its potential relevance to future flexible thermoelectric technologies as well.

Compared with conventional interface–engineering approaches, which predominantly rely on inorganic additives, the use of a conductive polymer such as PEDOT:PSS offers a fundamentally different interfacial design route by introducing an inexpensive, solution–processable, and flexibility–compatible organic phase. This polymer–based interface engineering provides opportunities for constructing tunable inorganic/organic interfaces that are distinct from those achieved by conventional approaches. In the present study, we aimed to promote more interfacial contact between Bi_2Te_3 and the conductive polymer to further enhance the energy filtering effect. To this end, we designed a reproducible one–pot chemical process, in which monomers were polymerized to form conductive polymers. These polymers were then immediately deposited onto Bi_2Te_3 to fabricate an inorganic/organic composite. Unlike our previous work, where Bi_2Te_3 and conductive polymers were mechanically blended, this one–pot chemical process enables the conductive polymer to be directly deposited onto the Bi_2Te_3 surface immediately after polymerization. This approach results in a more uniform distribution and finer dispersion of the polymer phase on Bi_2Te_3, promoting abundant interfacial contact and reducing agglomeration. The resulting composite exhibited a decoupled transport behavior between the Seebeck coefficient and electrical resistivity, characterized by a selective enhancement in the Seebeck coefficient. This improvement is attributed to the increased energy filtering effect originating from the more abundant interfacial contact. In addition, the composite exhibited a reduction in thermal conductivity, which is likely due to changes in phonon and charge carrier scattering at the newly formed interfaces with finely dispersed conductive polymer domains. These alterations in transport characteristics were confirmed not only through experimental material characterization but also through theoretical validation based on the single parabolic band model.

The composite exhibited excellent thermoelectric performance over a wide temperature range (300–550 K) applicable to Bi_2Te_3–based materials, achieving an average ZT of $\sim$ 1.15 and a maximum ZT of $\sim$ 1.31 at 477 K. This performance is highly competitive compared to those of state–of–the–art n–type Bi_2Te_3–based materials fabricated through various approaches. In addition to its outstanding thermoelectric performance, the composite offers several advantages, including the use of cost–effective polymer additives with potential for flexible device fabrication, a simple material composition, and an easily scalable fabrication process. These merits suggest that the composite can serve as a promising candidate for low–temperature n–type thermoelectric materials, with potential applications extending beyond conventional thermoelectric power generation to emerging areas such as energy harvesting.

2. Materials and methods

2.1. Sample fabrication

Elemental bismuth (Bi, 80 mmol, 99.99 %, Kojundo Chemicals) and tellurium (Te, 120 mmol, 99.99 %, Kojundo Chemicals) powders were mixed using an agate mortar and pestle. The blended powders were loaded into a quartz tube, sealed under vacuum, and heated in a rocking furnace at 1173 K (heating rate: 10 K min^{-1}). This temperature was maintained for 24 h to ensure complete reaction between Bi and Te. The resulting product was allowed to cool naturally to room temperature to yield a Bi_2Te_3 ingot. The Bi_2Te_3 ingot was then ground into powder using a Mortar Grinder Pulverisette 2 (Fritsch) and dispersed in distilled water under stirring to obtain a Bi_2Te_3 aqueous suspension. For in situ polymer integration, 3,4–ethylenedioxythiophene (EDOT, 0.151 mmol, 97 %, Sigma–Aldrich) and polystyrene sulfonate (PSS, 5.54×10^{-4} mmol, 18 wt% in H_2O, Sigma–Aldrich) were added to the Bi_2Te_3 aqueous suspension and stirred. Sodium persulfate ($Na_2S_2O_8$, 0.2 mmol, $\geq$98 %, Sigma–Aldrich), dissolved in distilled water, was then introduced dropwise into the aqueous suspension using a syringe to initiate oxidative polymerization of EDOT. This one–pot chemical process enabled simultaneous formation of PEDOT:PSS and its deposition onto the surface of Bi_2Te_3 (Fig. 1a). Following polymer integration, the precipitate was filtered, washed, and vacuum–dried to obtain the solid product (s–Bi_2Te_3/PEDOT:PSS, $\sim$99.5/0.5 w/w). For comparison, a Bi_2Te_3/PEDOT:PSS composite (BT/P) was also prepared by blending Bi_2Te_3 powder with pre–synthesized PEDOT:PSS via planetary dry ball milling (Fig. 1b), following our previous method [26,27]. The s–Bi_2Te_3/PEDOT:PSS (s–BT/P) prepared in the present study was compared with both the Bi_2Te_3/PEDOT:PSS (BT/P) and pristine Bi_2Te_3 to comprehensively evaluate its material properties and thermoelectric performance.

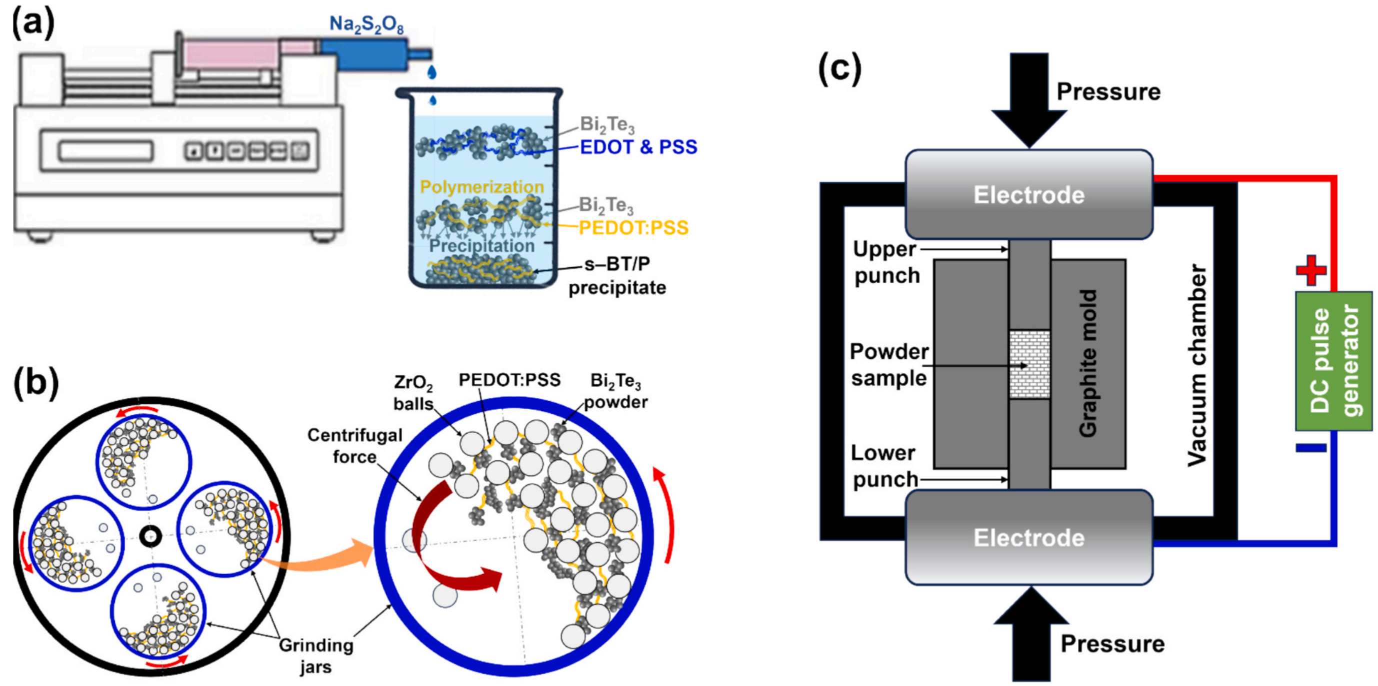

Fig. 1. Two different polymer integration processes: (a) A chemical oxidant ($Na_2S_2O_8$) was added dropwise using an infusion system to the aqueous suspension of Bi_2Te_3, EDOT, and PSS to initiate oxidative polymerization of EDOT. This process enabled simultaneous formation of PEDOT:PSS and its deposition onto the Bi_2Te_3 surface, thus affording the s–Bi_2Te_3/PEDOT:PSS (s–BT/P) precipitate; (b) Bi_2Te_3 powder was blended with pre–synthesized PEDOT:PSS via planetary dry ball milling to produce Bi_2Te_3/PEDOT:PSS (BT/P). (c) Each of the s–BT/P and BT/P samples was packed into a cylindrical graphite mold and compacted by spark plasma sintering.

Each of the s–BT/P, BT/P, and pristine Bi_2Te_3 powders (12 g each) was packed into a cylindrical graphite mold (outer diameter × height = 55 mm × 60 mm, inner hole = 12 mm) and consolidated using a spark plasma sintering (SPS) system (Dr. Sinter 632Lx, Fuji Electronic Industrial Co., Fig. 1c). SPS was carried out under an Ar atmosphere at 603 K and 100 MPa (heating rate: 100 K min^{-1}), with a holding time of 1 min, followed by natural cooling. The resulting products were cylindrical dense bulk specimens with dimensions of 12.0 mm in diameter and 13.8–14.1 mm in height.

2.2. Measurements and characterizations

X–ray diffraction (XRD) measurements were performed using a Miniflex II diffractometer (Rigaku) with Cu K_α radiation ($\lambda = 1.5406$ Å). XRD patterns were recorded over a 2θ range of 10–80° (step width: 0.02°, scan rate: 5° min^{-1}). Lattice parameters were calculated using the following equation derived from the combination of Bragg's law and the plane–spacing equation:

$$\sin^2\theta = \frac{\lambda^2}{4}\left[\frac{4}{3}\left(\frac{h^2+hk+k^2}{a^2}\right)+\frac{l^2}{c^2}\right] \tag{1}$$

In this equation, θ is the diffraction angle; a and c are the lattice constants; (hkl) are the Miller indices corresponding to the crystal plane; and $\lambda^2/4$ has a value of 0.594 $Å^2$ for Cu K_α radiation. X–ray photoelectron spectroscopy (XPS) was conducted using an ESCALAB 250Xi spectrometer equipped with a dual anode X–ray source (Mg K_α/Al K_α). The C 1 s peak at approximately 285 eV was used as the energy reference. Thermogravimetric analysis (TGA) was carried out using a PT1600 thermogravimeter (Linseis) in the temperature range of 300–950 K at a heating rate of 10 K min^{-1} under a mixed gas flow (Ar: 10 mL min^{-1}, air: 90 mL min^{-1}). The microstructures of the samples were examined using field–emission scanning electron microscopy (FE–SEM, JSM–7000F, Jeol) and transmission electron microscopy (TEM, Titan G2, FEI). TEM analysis was performed at an accelerating voltage of 300 kV to obtain high–resolution TEM (HR–TEM) micrographs. Fast Fourier transform (FFT) patterns were extracted from selected HR–TEM images to analyze crystallographic information in the frequency domain. Energy–dispersive X–ray spectroscopy (EDX) was also performed in STEM mode to correlate the elemental mapping profiles with the corresponding TEM analyses. Raman spectroscopy was performed using a commercial confocal Raman system (inVia Qontor, Renishaw) equipped with an Ar^+ laser and a CCD detector. A solid–state 532 nm excitation laser was used and the laser power was set to 0.25 mW (exposure time of 1 s with 100 cycles).

Bi_2Te_3 is known to exhibit crystallographic anisotropy, which leads to significant directional dependence in its thermoelectric transport properties. Therefore, all thermoelectric measurements were performed in the direction perpendicular to the pressing axis of the sintered specimens. The Seebeck coefficient (α) and electrical resistivity (ρ) were simultaneously measured in the temperature range of 300–550 K using a commercial thermoelectric measurement system (ZEM–3, Ulvac–Riko) at a heating rate of 10 K min^{-1}. The Hall coefficient was measured using a Hall effect measurement system (HMS–3000, Ecopia) based on the van der Pauw method to determine the carrier concentration (n). The Hall mobility (μ_H) was calculated from the relation $\mu_H = (ne\rho)^{-1}$, where e is the elementary charge (1.6×10^{-19}C). The total thermal conductivity (κ) was derived from the relation $\kappa = \lambda C_p d$, where λ is the thermal diffusivity, C_p is the specific heat capacity at constant pressure, and d is the mass density. λ was measured in the range of 300–550 K using a laser flash analyzer (LFA 447, Netzsch) at a heating rate of 10 K min^{-1}. C_p was evaluated using a differential scanning calorimeter (DSC 200, Netzsch), and d was determined based on the Archimedes principle. The sintered specimens showed d of 7.61 g cm^{-3} (pristine Bi_2Te_3) and 7.59 g cm^{-3} (BT/P and s–BT/P), corresponding to approximately 97 % of the theoretical density of Bi_2Te_3 (7.86 g cm^{-3} [33]). κ consists of three components: electronic (κ_e), lattice (κ_l), and bipolar (κ_b) thermal conductivities. κ_e was calculated using the Wiedemann–Franz law, $\kappa_e = LT/\rho$, where L is the Lorenz number. The sum of κ_l and κ_b was estimated by subtracting κ_e

from κ. Considering that the lattice thermal conductivity typically follows a linear T^{-1} dependence above the Debye temperature of Bi_2Te_3 (~165 K) [34], κ_l was estimated accordingly. This allowed for approximation of the bipolar contribution κ_b as well. The thermoelectric figure of merit (ZT) was calculated using the relation, $ZT = \alpha^2T/(\rho\kappa)$. The standard deviations from repeated measurements of the transport properties were primarily used to determine the error bars presented in this work. For parameters derived from analytical relations (such as κ_l and κ_b), the uncertainties were estimated by propagating the experimental and fitting–based errors of the relevant quantities.

3. Results and discussion

The XRD pattern of s–BT/P was nearly identical to those of BT/P and pristine Bi_2Te_3, all of which matched the typical diffraction peaks of rhombohedral Bi_2Te_3 (JCPDS card No. 15–0863) (Fig. 2a, left panel). Pristine PEDOT:PSS exhibited only a broad and weak peak near $2\theta = 25^\circ$, indicative of the amorphous characteristic of polymeric substances. s–BT/P showed no noticeable peak shift or distortion associated with PEDOT:PSS, consistent with the pattern observed for BT/P. To further verify whether s–BT/P underwent any structural changes, lattice parameters were calculated by applying the two most intense peaks, corresponding to the (015) and (1010) planes at 27.6° and 37.9°, respectively (Fig. 2a, right panel), to Eq. (1). As shown in Figs. 2b, s–BT/P exhibited no significant deviation in lattice parameters compared to pristine Bi_2Te_3, similar to BT/P. These XRD results suggest that no crystallographic change occurred in the Bi_2Te_3 phase, implying that the one–pot chemical process used for s–BT/P formation did not induce any chemical reaction between Bi_2Te_3 and PEDOT:PSS. High–resolution C 1 s XPS spectra were collected to investigate possible chemical changes in the PEDOT:PSS component across the samples (Fig. 2c). The spectrum of pristine PEDOT:PSS consisted of a main peak at 284.6 eV and two shoulder peaks at 286.5 and 288.6 eV. Deconvolution revealed that the main peak comprised two characteristic components: C=C bonds in PEDOT (red, 284.4 eV) and C–C bonds in PSS (green, 285.0 eV) [35]. The shoulder peaks were assigned to C–O/C–S bonds in PEDOT:PSS (blue, 286.5 eV) and residual bonds (purple, 288.6 eV), attributed to polymeric ring cleavage due to oxidation and sulfurization of C–O/C–S bonds [35]. Since carbon is the main element constituting the backbone and ring structures of PEDOT:PSS, its signal serves as a useful indicator of chemical integrity. However, in s–BT/P, the PEDOT:PSS fraction is significantly smaller than that of the Bi_2Te_3 component (s–BT/P ~ 99.5/0.5 w/w, see section 2.1), resulting in a markedly lower C 1 s signal intensity compared to pristine PEDOT:PSS. The main peak positions of s–BT/P, BT/P, and pristine PEDOT:PSS were nearly identical, indicating negligible shifts in the binding energies of the C=C bonds in PEDOT and C–C bonds in PSS. These results suggest that the PEDOT:PSS component in s–BT/P remained chemically unchanged, not only relative to BT/P but also to pristine PEDOT:PSS. TGA analysis revealed that s–BT/P exhibited an overall thermal decomposition pattern similar to that of pristine Bi_2Te_3, with a sharp weight loss occurring near 850 K due to the thermal collapse and decomposition of the Bi_2Te_3 structure (Fig. 2d, upper panel). However, unlike pristine Bi_2Te_3, s–BT/P displayed additional weight losses in the temperature ranges of 477–585 K and 585–830 K (Fig. 2d, upper panel, inset). These additional decomposition features of s–BT/P closely resembled the thermal degradation behavior of both BT/P and pristine PEDOT:PSS in the corresponding temperature ranges (Fig. 2d, lower panel). In pristine PEDOT:PSS, these losses account for approximately 80 % of the total weight, primarily arising from the pyrolysis of the PSS and PEDOT molecular frameworks [36]. The presence

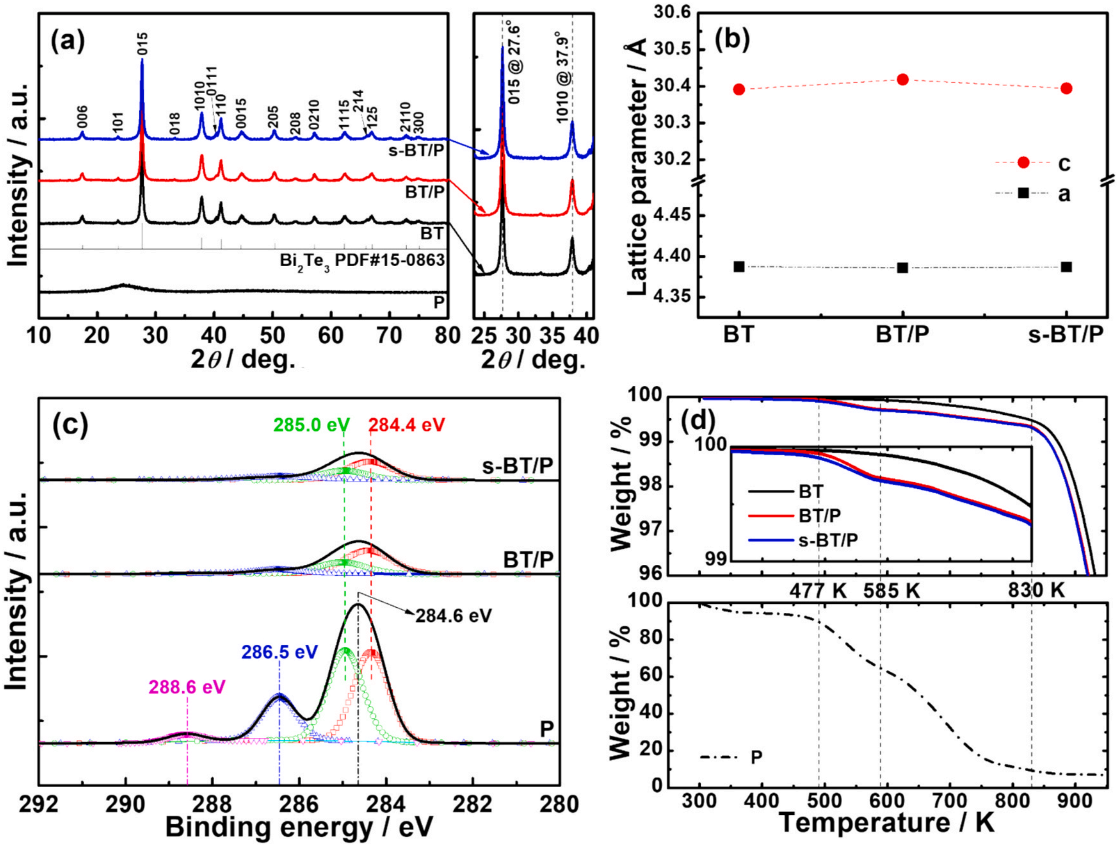

Fig. 2. Material characterizations of s–Bi_2Te_3/PEDOT:PSS (s–BT/P) and Bi_2Te_3/PEDOT:PSS (BT/P), compared with pristine PEDOT:PSS (P) and Bi_2Te_3 (BT): (a) X–ray diffraction (XRD) patterns over the 2θ range of 10–80° (left), with a magnified view of the 25–40° region (right); (b) calculated lattice parameters; (c) high–resolution X–ray photoelectron spectroscopy (XPS) spectra of C 1 s; (d) thermogravimetric analysis (TGA) curves in the temperature range of 300–950 K, with an enlarged view of 350–830 K in the inset.

of similar decomposition characteristics in s–BT/P suggests that the PEDOT:PSS component retains a molecular structure comparable to its pristine form. The material characterization results (XRD, XPS, and TGA) indicate that no chemical reaction occurred between Bi_2Te_3 and PEDOT:PSS during the one–pot chemical process. The two components are likely distributed in distinct domains with interfacial contact.

Based on SEM analysis (Fig. 3), pristine Bi_2Te_3 particles were generally larger than pristine PEDOT:PSS particles, but both pristine samples exhibited similarly irregular morphologies. Consequently, individual components in BT/P and s–BT/P could not be clearly distinguished in SEM images. Low–magnification TEM images (Fig. 4a1, 4b1) revealed particles with contrasting brightness in both BT/P and s–BT/P. According to HR–TEM analysis (Fig. 4a2, 4b2), the darker particles exhibited well–defined lattice fringes corresponding to periodic atomic arrangements, while the brighter ones lacked such ordering. The measured lattice spacings of 3.21 and 3.20 Å were identified as the (015) and $(10\overline{5})$ planes of $R\overline{3}m$ Bi_2Te_3 along the $[5\overline{5}1]$ zone axis, as confirmed by the corresponding FFT patterns (insets of Fig. 4a2 and 4b2). STEM/EDX mapping further supported this assignment (Fig. 4a3–4a6, 4b3–4b6): the darker particles showed strong bismuth (Fig. 4a4, 4b4) and tellurium (Fig. 4a5, 4b5) signals, consistent with the HR–TEM results indicating crystalline Bi_2Te_3. In contrast, the brighter particles exhibited dominant carbon signals (Fig. 4a6, 4b6), suggesting they were composed of PEDOT:PSS, whose main elemental component is carbon. These results indicate that Bi_2Te_3 and PEDOT:PSS form interfacial domains in both s–BT/P and BT/P and that the PEDOT:PSS particles in s–BT/P are smaller than those in BT/P. Additional datasets obtained from other regions showed the same microstructural tendencies (Fig. S1, Supplementary Material). This size reduction likely results from the one–pot chemical process, in which the polymerization of PEDOT:PSS is kinetically regulated and occurs in situ on Bi_2Te_3 surfaces, leading to finer dispersion. By contrast, BT/P was prepared by dry ball milling of pristine Bi_2Te_3 and PEDOT:PSS, making PEDOT:PSS aggregation more likely and resulting in relatively larger and less–dispersed particles.

The thermoelectric transport properties of s–BT/P and BT/P were compared with those of pristine Bi_2Te_3. All samples exhibited increasing electrical resistivity (ρ) with temperature, indicating degenerate semiconducting behavior (Fig. 5a). The ρ values of s–BT/P and BT/P were comparable to that of pristine Bi_2Te_3, whereas their Seebeck coefficients (α) were significantly higher (Fig. 5b). These results suggest a notable decoupling between ρ and α in s–BT/P and BT/P, compared to pristine Bi_2Te_3. s–BT/P and BT/P showed slightly lower carrier concentrations (n) than pristine Bi_2Te_3 (Fig. 5c), which can be attributed to a mild electron–depletion effect at the interfaces between Bi_2Te_3 and PEDOT:PSS components arising from their work function difference (Fig. S2, Supplementary Material). Although s–BT/P and BT/P had lower n than pristine Bi_2Te_3, their Hall mobilities (μ_H) were higher (Fig. 5c), resulting in overall resistivities similar to that of the pristine sample. The typical simultaneous increase in ρ and α with decreasing n was not observed (Fig. 5a–c). To explain the selective enhancement in α, the density of states effective mass (m^*) was considered. According to the following equation:

$$\alpha = \frac{8\pi^2 k_B^2}{3eh^2} m^* T \left(\frac{\pi}{3n}\right)^{\frac{2}{3}} \tag{2}$$

where k_B is the Boltzmann constant, e is the elementary charge, and h is Planck's constant. Expressing m^* relative to the free electron mass (m_0), both s–BT/P and BT/P exhibited clearly increased m^* values compared to that of pristine Bi_2Te_3 (Fig. 5c). The presence of interfacial potential barriers in BT/P, known to induce energy filtering effects [26,27], was further quantified in this study by ultraviolet photoelectron spectroscopy (UPS) measurements. The extracted barrier height ($\Delta\Phi$) and the corresponding UPS analysis are provided in Supplementary Material (Fig. S2, S3). Based on the electrical transport trends in Fig. 5a–c, similar energy filtering is expected in s–BT/P. The weighted mobility (μ_w), defined as $\mu(m^*/m_0)^{3/2}$, is a more suitable parameter than μ_H for evaluating charge transport behavior influenced by energy filtering [37]. Both s–BT/P and BT/P exhibited significantly higher μ_w than pristine Bi_2Te_3 (Fig. 5c), strongly supporting the presence of energy filtering effects, which preferentially transmit high–energy carriers while filtering out low–energy ones (Fig. 6a). Notably, s–BT/P exhibited even higher μ_w than BT/P, which can be ascribed to more active energy filtering possibly arising from the increased interfacial domains, enabled by the finer dispersion of PEDOT:PSS as discussed earlier and as described in Fig. 6b. μ_w was also calculated from the experimental ρ and α values based on the single parabolic band model, assuming acoustic phonon scattering as the dominant mechanism. The temperature–dependent μ_w was determined by: [38].

$$\mu_w = \frac{3}{8\pi e\rho F_0(\eta)} \left(\frac{h^2}{2m_0 k_B T}\right)^{\frac{3}{2}} \tag{3}$$

where $F_0(\eta)$ is the zeroth–order Fermi integral:

$$F_n(\eta) = \int_0^\infty \frac{x^n}{1+\exp(x-\eta)} dx \tag{4}$$

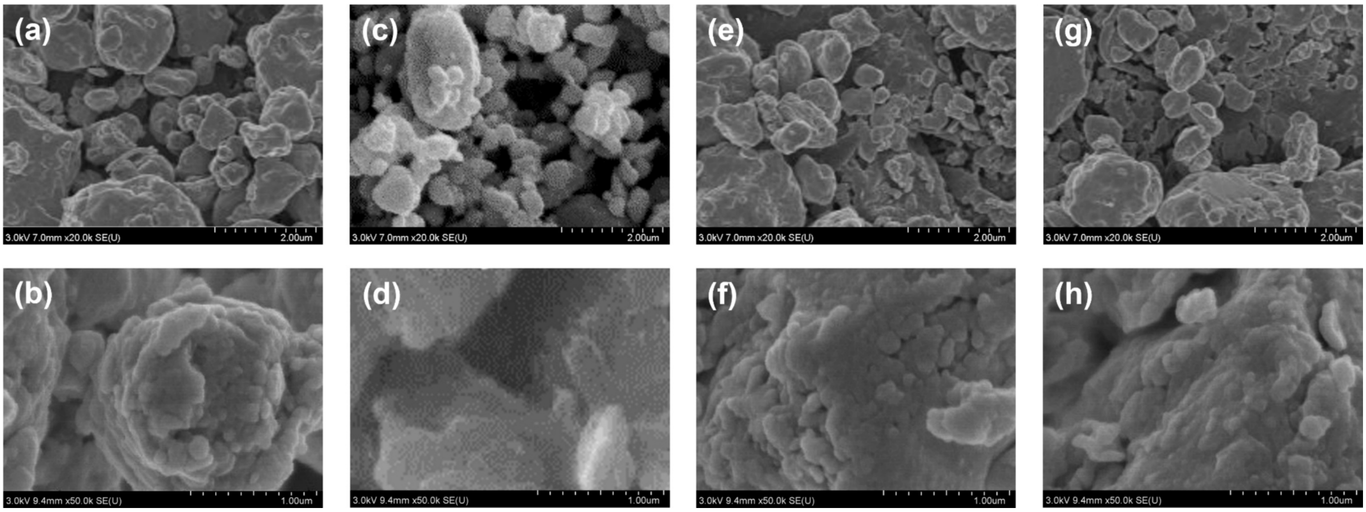

Fig. 3. SEM micrographs of each sample with different resolutions: (a,b) pristine Bi_2Te_3, (c,d) pristine PEDOT:PSS, (e,f) Bi_2Te_3/PEDOT:PSS (BT/P), and (g,h) s–Bi_2Te_3/PEDOT:PSS (s–BT/P).

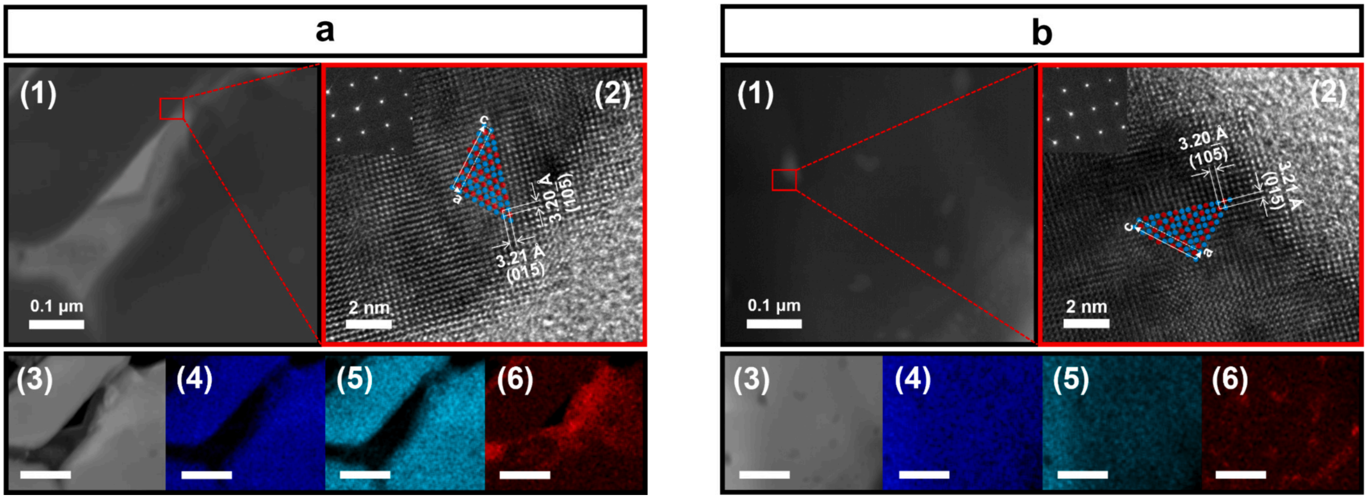

Fig. 4. TEM and STEM characterization of Bi_2Te_3/PEDOT:PSS (BT/P, a) and s–Bi_2Te_3/PEDOT:PSS (s–BT/P, b). Low–magnification TEM images (a1, b1). High–resolution TEM (HR–TEM) images with corresponding FFT insets (a2, b2), showing the lattice structure and atomic arrangement of Bi_2Te_3 (red: Bi, blue: Te). STEM images (a3, b3) with EDX elemental maps of Bi (a4, b4), Te (a5, b5), and C (a6, b6). All STEM/EDX images use a 0.2 μm scale bar. (For interpretation of the references to colour in this figure legend, the reader is referred to the web version of this article.)

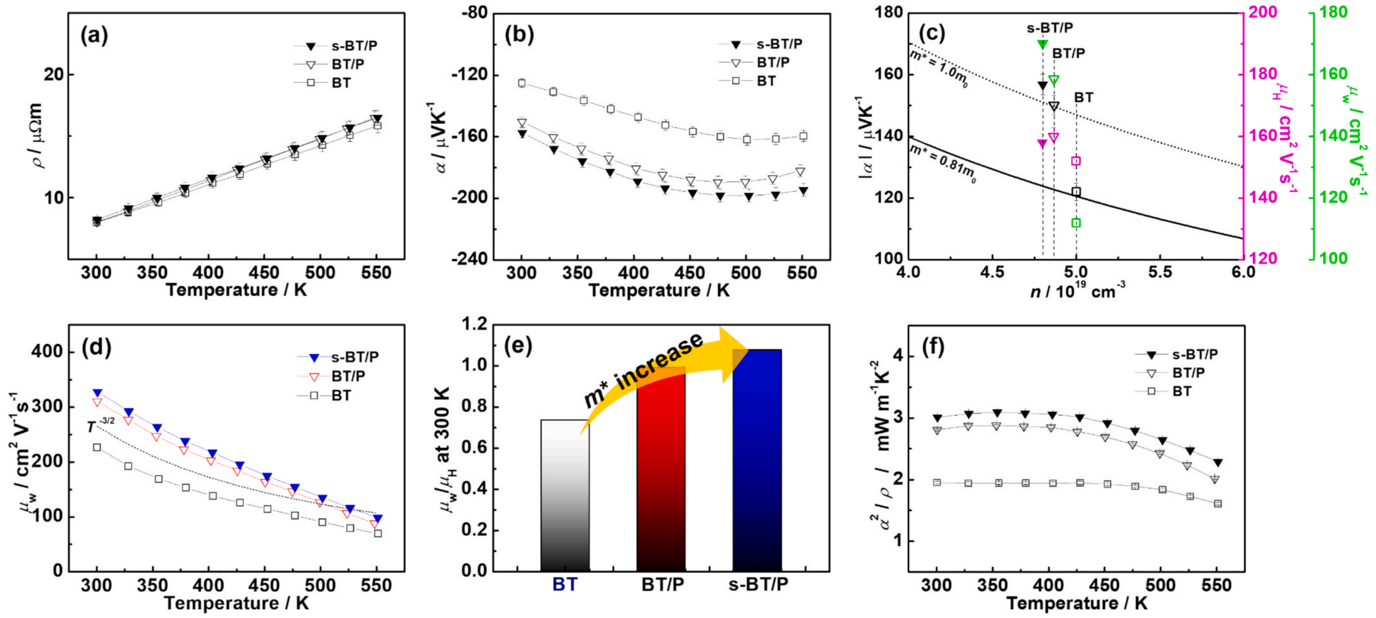

Fig. 5. Thermoelectric transport properties of s–Bi_2Te_3/PEDOT:PSS (s–BT/P) and Bi_2Te_3/PEDOT:PSS (BT/P) compared with pristine Bi_2Te_3 (BT): temperature dependence of (a) electrical resistivity (ρ) and (b) Seebeck coefficient (α), (c) Seebeck coefficient as a function of carrier concentration (n) accompanied by the density of states effective mass (m^*) at 300 K, together with Hall mobility (μ_H) and weighted mobility (μ_w), (d) μ_w/μ_H ratio at 300 K, temperature dependence of (e) μ_w and (f) power factor (α^2/ρ).

The reduced chemical potential η was obtained using the following equation:

$$\alpha = \pm\frac{k_B}{e}\left(\frac{2F_1(\eta)}{F_0(\eta)} - \eta\right) \tag{5}$$

The calculated μ_w (Fig. 5d) at 300 K showed trends consistent with those presented in Fig. 5c. The observed $T^{-3/2}$ dependence of μ_w is indicative of dominant acoustic phonon scattering [39]. The ratio μ_w/μ_H ($\propto (m^*)^{3/2}$), calculated at 300 K, further confirmed the highest m^* in s–BT/P (Fig. 5e). The observed trends in α aligned well with those of m^* and μ_w, whereas ρ showed minimal variation across the samples (Fig. 5a–d). These results indicate that s–BT/P exhibits stronger energy filtering effects, which in turn lead to its superior power factor (α^2/ρ) compared to both BT/P and pristine Bi_2Te_3 (Fig. 5f).

As shown in Fig. 7a, both s–BT/P and BT/P exhibited lower total thermal conductivity (κ) than pristine Bi_2Te_3 over the entire temperature range. The electronic thermal conductivity (κ_e) for each sample was calculated using the Wiedemann–Franz law with the Lorenz number (L), which was estimated from the measured α using the empirical relation $L = 1.5 + \exp(-|\alpha|/116)$ [40]. κ_e showed small differences among the samples (Fig. 7b), consistent with their comparable ρ (Fig. 5a). The quantity $\kappa - \kappa_e$, representing the sum of lattice (κ_l) and bipolar (κ_b) thermal conductivities, is shown in Fig. 7c. To extract κ_l, we used the commonly adopted relation $\kappa_l = aT^{-1} + b$. The T^{-1} dependence originates from Umklapp phonon–phonon scattering at elevated temperatures, while the constant term b accounts for temperature–independent contributions such as boundary, defect, or interface scattering [41–43]. The resulting fitting parameters for each sample are summarized in

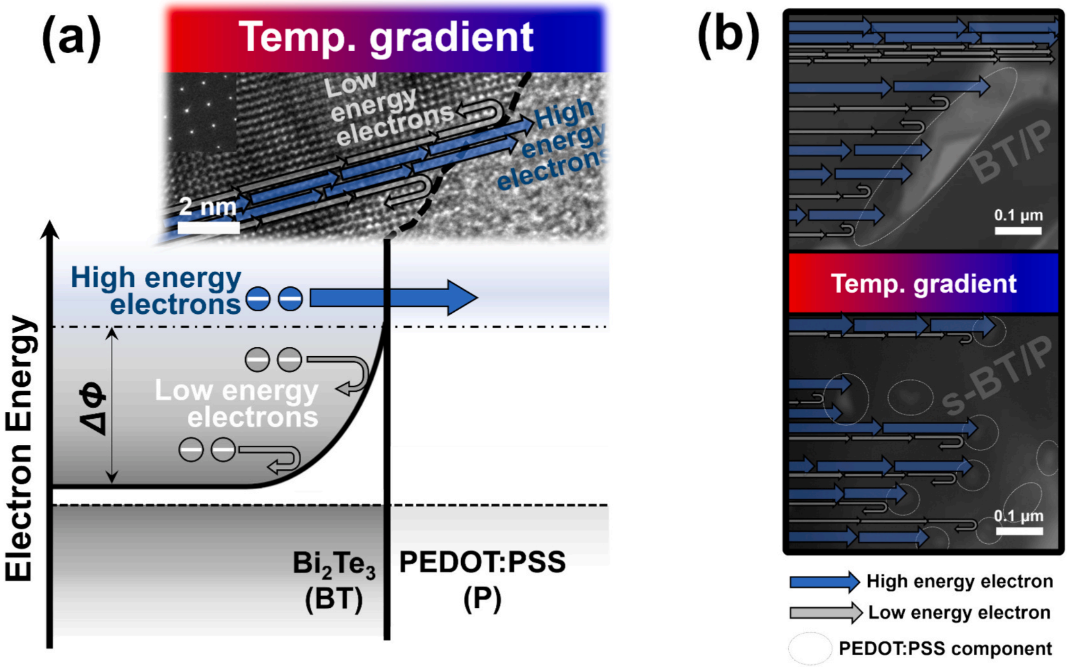

Fig. 6. (a) Interfacial potential barrier ($\Delta\Phi$) between the components in Bi_2Te_3/PEDOT:PSS (BT/P) and s–Bi_2Te_3/PEDOT:PSS (BT/P), quantified by a band–bending potential, which may induce an energy filtering effect (energy–dependent carrier scattering); (b) illustration of energy filtering using the HR–TEM images of BT/P and s–BT/P.

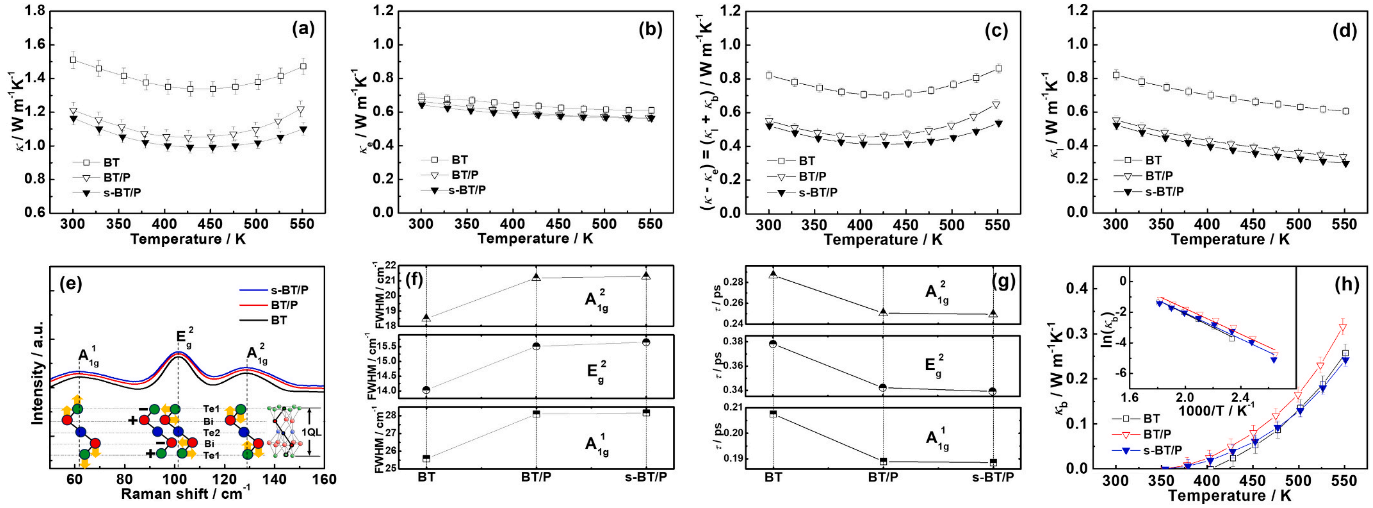

Fig. 7. Thermoelectric and physical properties of s–Bi_2Te_3/PEDOT:PSS (s–BT/P) and Bi_2Te_3/PEDOT:PSS (BT/P) compared with pristine Bi_2Te_3 (BT): temperature dependence of (a) total thermal conductivity (κ), (b) electronic thermal conductivity (κ_e), (c) difference ($\kappa - \kappa_e$), and (d) lattice thermal conductivity (κ_l); (e) Raman spectra at room temperature and relevant phonon modes (A^1_{1g}, E^2_g, and A^2_{1g}) in the quintuple layer (QL) of Bi_2Te_3 lattice structure (inset); corresponding (f) full–width half–maximum (FWHM) and (g) phonon relaxation time (τ), derived from the phonon modes; temperature dependence of (h) bipolar thermal conductivity (κ_b) with $\ln(\kappa_b)$ plotted versus T^{-1} in the inset.

Fig. S4 (Supplementary Material). Both s–BT/P and BT/P exhibited significantly lower κ_l than pristine Bi_2Te_3 (Fig. 7d), likely owing to enhanced phonon scattering at the interfaces between Bi_2Te_3 and PEDOT:PSS components. To experimentally examine the phonon dispersions of each sample, Raman spectroscopy was conducted at room temperature (Fig. 7e). The rhombohedral Bi_2Te_3 structure is known to consist of three quintuple layers (QLs) stacked via van der Waals interactions [44]. Each QL contains five atomic layers (Te^1–Bi–Te^2–Bi–Te^1) alternately arranged (Fig. 7e, inset), where lattice vibrations of the atoms occur. All samples exhibited three Raman active vibrational modes, A^1_{1g} (ca. 60 cm^{-1}), E^2_g (ca. 100 cm^{-1}), and A^2_{1g} (ca. 130 cm^{-1}), which are assigned to longitudinal (A^1_{1g}, A^2_{1g}) and transverse (E^2_g) vibrations of Bi–Te^1 in the QL. The full–width at half–maximum (FWHM) of the observed vibration modes was analyzed to evaluate the phonon relaxation time (τ), using the energy–time uncertainty relation:

$$FWHM = \frac{h}{2\pi\tau} \tag{6}$$

where h is the Planck constant. The FWHM of the E^2_g vibrational mode in s–BT/P and BT/P was larger than that of pristine Bi_2Te_3 (Fig. 7f; Fig. S5, Supplementary Material). Similar broadening was observed for the A^1_{1g} and A^2_{1g} modes. Consequently, the phonon relaxation times (τ) of s–BT/P and BT/P were smaller than that of pristine Bi_2Te_3 (Fig. 7g). Because τ is inversely proportional to the phonon relaxation rate, the reduced τ values for s–BT/P and BT/P indicate increased phonon scattering in both longitudinal and transverse directions. This enhanced scattering is ascribed to the interfaces between the Bi_2Te_3 and PEDOT:PSS components. This interpretation is further supported by XRD and XPS analyses, which show no grain size variation, microstrain, or defect–related chemical changes upon polymer integration, indicating that these structural factors are unlikely to contribute to the observed FWHM broadening. Accordingly, the reduced κ_l in both samples is consistent with the scattering of phonon modes observed in the Raman spectra. The difference in κ_l between s–BT/P and BT/P was relatively small (Fig. 7d). TEM analysis revealed that s–BT/P contained finely dispersed PEDOT:PSS particles embedded within Bi_2Te_3 grains, while BT/P featured relatively larger PEDOT:PSS domains located at Bi_2Te_3 grain boundaries. Considering the phonon scattering mechanisms closely related to phonon mean free path, namely, atomic point–defect scattering, nanoprecipitate scattering, and grain boundary scattering [45], s–BT/P is expected to promote phonon scattering in the intermediate regime (<100 nm) via nanoprecipitate scattering. In contrast, BT/P is likely to promote scattering of long mean free path phonons (0.1–10 μm) through grain boundary scattering. The similarity in κ_l between s–BT/P and BT/P likely stems from their selective engagement in distinct phonon scattering regimes, each effectively targeting different phonon mean free path ranges.

The temperature dependence of κ_l in all samples exhibited a distinctly different trend from that of $\kappa - \kappa_e$, which can be attributed to the narrow bandgap of Bi_2Te_3–based materials. This indicates that thermal excitation of minority carriers becomes increasingly significant at elevated temperatures, and thus their contribution to the total thermal conductivity must be considered. Because $\kappa - \kappa_e$ equals the sum of κ_l and κ_b as explained earlier, κ_b, which arises from the transport of thermally generated minority carriers, was extracted by subtracting both κ_e and κ_l from κ (Fig. 7h). As temperature increased, κ_b rose exponentially in all samples. The bipolar onset appeared at lower temperatures for s–BT/P and BT/P than for pristine Bi_2Te_3, likely due to the thermal

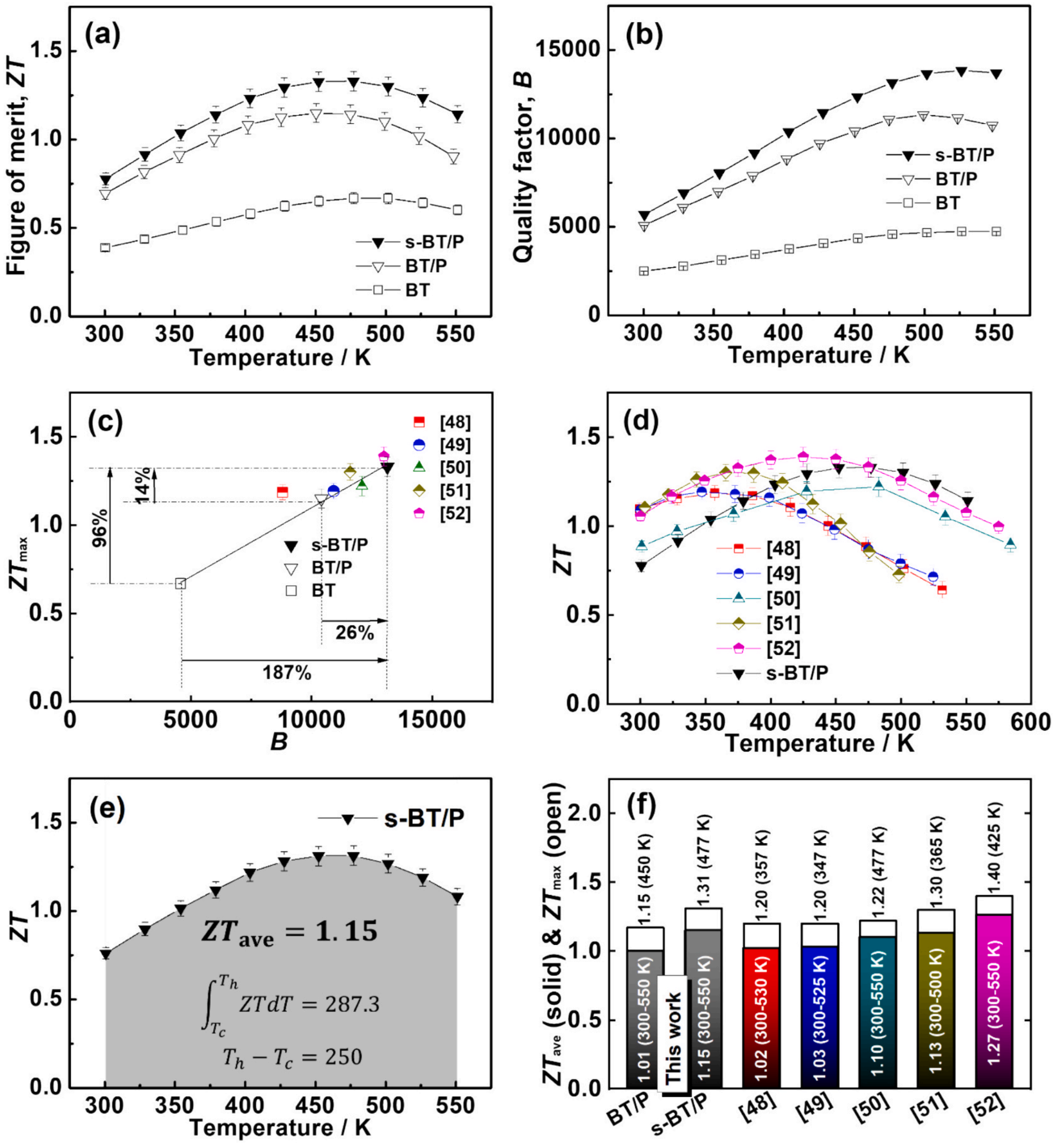

Fig. 8. Temperature–dependent (a) quality factor (B) and (b) figure of merit (ZT) for s–Bi_2Te_3/PEDOT:PSS (s–BT/P) compared to those for pristine Bi_2Te_3 (BT) and Bi_2Te_3/PEDOT:PSS (BT/P), (c) maximum ZT (ZT_{max}) versus B for s–BT/P compared to that for BT, BT/P, and recently reported n–type Bi_2Te_3–based materials [48–52], (d) temperature–dependent ZT for s–BT/P compared to the Bi_2Te_3–based materials, (e) average ZT (ZT_{ave}) of s–BT/P, derived by integrating the ZT curves over 300–550 K using the equation $ZT_{\mathrm{ave}} = \frac{1}{T_h - T_c}\int_{T_c}^{T_h} ZTdT$, and (f) ZT_{ave} comparison in a similar temperature range along with ZT_{max} of each material.

excitation of minority carriers (holes) originating from the PEDOT:PSS phase. Notably, κ_b in s–BT/P increased more slowly with temperature than in BT/P, approaching that of pristine Bi_2Te_3 at elevated temperatures. Although κ_b is known to depend on the bandgap energy (E_g) following the relation $\kappa_b \propto \exp(-E_g/k_BT)$, the similar slopes of the $\ln(\kappa_b)$ versus T^{-1} plots (inset of Fig. 7h) indicate comparable bandgap energies across the samples. Therefore, the observed differences in κ_b are not attributed to variations in E_g. κ_b is also affected by microstructural features such as defects, nanoinclusions, and grain boundaries, which can suppress minority carrier transport [46]. As discussed earlier, s–BT/P contains smaller and more finely dispersed PEDOT:PSS domains than BT/P, and these microstructural differences likely contribute to suppressing bipolar conduction. This accounts for the slower increase in κ_b with temperature observed in s–BT/P. This trend is also consistent with the higher Seebeck coefficient at elevated temperatures and the enhanced weighted mobility observed in s–BT/P (Figs. 5b and 5c), both of which are commonly used experimental indicators of suppressed bipolar conduction. A follow–up study is currently underway to theoretically elucidate these κ_b differences via separate weighted mobility calculations for majority and minority carriers based on a two–band model.

Both s–BT/P and BT/P exhibited significantly enhanced ZT values compared to pristine Bi_2Te_3 over the entire temperature range (Fig. 8a), achieving considerably higher maximum ZT (ZT_{max}) values than pristine Bi_2Te_3. As discussed in the previous section, improvements in electrical properties and reductions in thermal conductivity contributed to the substantial increase in ZT. s–BT/P exhibited higher ZT values than BT/P across the temperature range, primarily due to the selective enhancement in α. This enhancement is attributed to an increased number of energy filtering interfaces in s–BT/P, likely resulting from the reduced particle size and improved dispersion of PEDOT:PSS domains achieved via the one–pot chemical process. The relative ZT enhancement of s–BT/P became more pronounced at higher temperatures, and its ZT_{max} shifted toward higher temperature compared to that of BT/P. This trend can be ascribed to the suppressed bipolar conduction behavior in s–BT/P, as evidenced by the temperature dependence of α and κ_b (Figs. 5b and 7h).

The quality factor (B), proposed within the framework of the single parabolic band model, serves as an additional parameter for evaluating thermoelectric performance and is calculated as follows:

$$B = 9\frac{\mu_w}{\kappa_l}\left(\frac{T}{300}\right)^{\frac{5}{2}} \tag{7}$$

A larger B value generally corresponds to a higher ZT, making B a useful indicator for assessing thermoelectric materials [47]. The significance of B lies in its ability to provide a straightforward guideline for identifying promising thermoelectric materials, without the need to evaluate all individual transport parameters (α, ρ, κ). Specifically, materials with high μ_w and low κ_l, which are relatively independent of each other, are expected to exhibit superior thermoelectric performance. The temperature dependence of B for all samples (Fig. 8b) showed a similar trend to that of ZT (Fig. 8a), both increasing with temperature, reaching a maximum at elevated temperatures, and then gradually decreasing, and s–BT/P exhibited the highest B across the entire temperature range. When plotting ZT_{max} as a function of B (Fig. 8c), a linear increase in ZT_{max} with increasing B was observed, further confirming the notable correlation between the two parameters. To examine this relationship, ZT_{max} and B values of recently reported high–performance n–type Bi_2Te_3–based materials (namely $Bi_2Te_{2.79}Se_{0.21}$ [48], $Cu_{0.01}Bi_{1.985}Y_{0.015}Te_{2.7}Se_{0.3}$ [49], $Bi_2Te_{2.4}Se_{0.6}$ [50], $Bi_2Te_{2.4}Se_{0.6}$ incorporating TiO_2 nanoparticles ($Bi_2Te_{2.4}Se_{0.6}$ + TiO_2) [51], and $Bi_{1.8}Sb_{0.2}Te_{2.7}Se_{0.3}$ with excess Te ($Bi_{1.8}Sb_{0.2}Te_{2.7}Se_{0.3}$ + Te) [52]) were also plotted for comparison (Fig. 8c). These reference materials, all based on n–type $Bi_2Te_xSe_{3-x}$ systems, achieve high ZT values through texture modification via hot deformation and liquid–state manipulation [48,50] or microstructural engineering with secondary/tertiary inorganic phases [49,51,52]. The μ_w and κ_l values used to derive their B factors are provided in Supplementary Material (Table S1). The reference materials generally follow the linear proportionality between ZT_{max} and B, indicating that higher B values tend to yield higher ZT_{max}. Although s–BT/P exhibited a higher B value than the reference materials, its ZT_{max} was comparable to that of $Bi_2Te_{2.4}Se_{0.6}$ + TiO_2 [51] and slightly lower than that of $Bi_{1.8}Sb_{0.2}Te_{2.7}Se_{0.3}$ + Te [52]. Such minor deviations from the linear relationship are likely due to compositional and microstructural variations among the different materials, which B alone cannot fully capture.

The temperature dependence of ZT for s–BT/P was compared with that of the reference Bi_2Te_3–based materials (Fig. 8d). The reference materials exhibited distinct temperature ranges, in which their thermoelectric performance was maximized. Compared with s–BT/P, $Bi_2Te_{2.79}Se_{0.21}$ [48], $Cu_{0.01}Bi_{1.985}Y_{0.015}Te_{2.7}Se_{0.3}$ [49], and $Bi_2Te_{2.4}Se_{0.6}$ + TiO_2 [51] showed relatively high ZT values below ca. 400 K, but their ZT rapidly decreased above this temperature. $Bi_2Te_{2.4}Se_{0.6}$ [50] exhibited a similar temperature–dependent trend to s–BT/P, though its ZT values were lower throughout most of the measured range. $Bi_{1.8}Sb_{0.2}Te_{2.7}Se_{0.3}$ + Te [52] maintained consistently high ZT values across the entire temperature range, suggesting that it would yield the highest average ZT (ZT_{ave}) among the compared materials. The ZT_{ave} for each sample over the entire temperature range (300–550 K) was calculated using the following equation:

$$ZT_{ave} = \frac{1}{T_h - T_c}\int_{T_c}^{T_h} ZTdT \tag{8}$$

where T_c and T_h are 300 and 550 K, respectively. The s–BT/P composite recorded ZT_{ave} of approximately 1.15 (Fig. 8e), representing improvements of about twofold and 14 % compared with pristine Bi_2Te_3 and BT/P, respectively (Fig. S6, Supplementary Material). The ZT_{ave} of s–BT/P was also compared with those of the reference materials (Fig. 8f), whose ZT_{ave} values were derived as detailed in Supplementary Material (Fig. S7). The ZT_{ave} of s–BT/P outperformed those of $Bi_2Te_{2.79}Se_{0.21}$, $Cu_{0.01}Bi_{1.985}Y_{0.015}Te_{2.7}Se_{0.3}$, and $Bi_2Te_{2.4}Se_{0.6}$ [48–50], while it was comparable to that of $Bi_2Te_{2.4}Se_{0.6}$ + TiO_2 [51] or somewhat lower than that of $Bi_{1.8}Sb_{0.2}Te_{2.7}Se_{0.3}$ + Te [52]. The similar or somewhat lower ZT_{ave} of s–BT/P compared to these two materials [51,52] can be attributed to its relatively reduced performance at lower temperatures (Fig. 8d), despite maintaining high thermoelectric performance at higher temperatures within the measurement range. Efforts are currently underway to selectively improve the low–temperature performance of s–BT/P while maintaining its high thermoelectric performance at elevated temperatures. $Bi_{1.8}Sb_{0.2}Te_{2.7}Se_{0.3}$ + Te, which achieved the highest ZT among n–type Bi_2Te_3–based materials reported to date, was synthesized via intentional liquid–phase sintering to form an excess Te phase. However, this material requires precise control of a complex quaternary stoichiometry and additional expensive elements such as Sb or Te. s–BT/P offers simpler processability without compositional complexity, cost advantages stemming from the use of conductive polymer, and potential compatibility with flexible device fabrication, suggesting its greater utility for practical thermoelectric applications.

4. Conclusion

In summary, a thermoelectric composite (s–Bi_2Te_3/PEDOT:PSS, s–BT/P) was successfully fabricated via a simple one–pot chemical process, enabling in situ integration of PEDOT:PSS with Bi_2Te_3. This interfacial design strategy produced finely dispersed PEDOT:PSS domains and more interfacial contacts, which collectively optimized carrier and phonon transport across the composite. Compared with pristine Bi_2Te_3 and mechanically mixed Bi_2Te_3/PEDOT:PSS (BT/P), s–BT/P exhibited a distinct decoupling of electrical resistivity and Seebeck coefficient through enhanced energy filtering effects, while effectively suppressing bipolar conduction at elevated temperatures. s–BT/P also exhibited substantial reductions in lattice and bipolar thermal conductivities due to enhanced phonon scattering and suppressed minority carrier transport. As a result, s–BT/P achieved a maximum *ZT* of ∼ 1.31 and an average *ZT* of ∼ 1.15 within 300–550 K, surpassing those of pristine Bi_2Te_3 and BT/P. The combination of facile processability, cost efficiency, and enhanced thermoelectric performance highlights the potential of in situ polymer integration as a versatile route to design practical and scalable thermoelectric materials.

CRediT authorship contribution statement

Cham Kim: Writing – review & editing, Writing – original draft, Validation, Supervision, Project administration, Methodology, Investigation, Funding acquisition, Formal analysis, Data curation, Conceptualization. **Changwoo Lee:** Visualization, Software, Resources, Investigation, Formal analysis, Data curation. **Hyun-Sik Kim:** Validation, Supervision, Software, Methodology, Investigation, Data curation, Conceptualization. **David Humberto Lopez:** Investigation, Formal analysis, Data curation.

Declaration of competing interest

The authors declare that they have no known competing financial interests or personal relationships that could have appeared to influence the work reported in this paper.

Acknowledgements

This work was supported by the DGIST R&D Program of the Ministry of Science, ICT and Technology of Korea (25–ET–02). This work was also supported by the National Research Foundation of Korea (NRF) grant funded by the Korean government (MSIT) (No. 2021R1F1A1045583, RS–2025–23523679).

Appendix A. Supplementary data

Supplementary data to this article can be found online at https://doi.org/10.1016/j.matdes.2026.115454.

Data availability

Data will be made available on request.

References

[1] S.B. Riffat, X. Ma, Thermoelectrics: a review of present and potential applications, Appl. Therm. Eng. 23 (2003) 913–935, https://doi.org/10.1016/s1359-4311(03)00012-7.

[2] P.A. Finn, C. Asker, K. Wan, E. Bilotti, O. Fenwick, C.B. Nielsen, Thermoelectric materials: current status and future challenges, Front. Electron. Mater. 1 (2021) 677845, https://doi.org/10.3389/femat.2021.677845.

[3] G.J. Snyder, T.S. Ursell, Thermoelectric efficiency and compatibility, Phys. Rev. Lett. 91 (2003) 148301, https://doi.org/10.1103/PhysRevLett.91.148301.

[4] R. Kumar, R. Bhatt, A. Tewary, A.K. Debnath, P. Bhatt, N. Mani, P. Jha, P. Patro, S. Bhattacharya, M. Pathak, M.K. Khan, A. Singh, K.P. Muthe, Synergistic effect of Zn doping on thermoelectric properties to realize a high figure–of–merit and conversion efficiency in Bi2-xZnxTe3 based thermoelectric generators, J. Mater. Chem. C 10 (2022) 7970–7979, https://doi.org/10.1039/d1tc06118f.

[5] D. Zhao, A. Würger, X. Crispin, Ionic thermoelectric materials and devices, J. Energy Chem. 61 (2021) 88–103, https://doi.org/10.1016/j.jechem.2021.02.022.

[6] E. Witkoske, X. Wang, J. Maassen, M. Lundstrom, Universal behavior of the thermoelectric figure of merit, zT, vs. quality factor, Mater. Today Phys. 8 (2019) 43–48, https://doi.org/10.1016/j.mtphys.2018.12.005.

[7] J. Wei, L. Yang, Z. Ma, P. Song, M. Zhang, J. Ma, F. Yang, X. Wang, Review of current high–ZT thermoelectric materials, J. Mater. Sci. 55 (2020) 12642–12704, https://doi.org/10.1007/s10853-020-04949-0.

[8] J. An, M.K. Han, S.J. Kim, Synthesis of heavily Cu–doped Bi2Te3 nanoparticles and their thermoelectric properties, J. Solid State Chem. 270 (2019) 407–412, https://doi.org/10.1016/j.jssc.2018.11.024.

[9] F. Wu, H.Z. Song, J.F. Jia, X. Hu, Effects of Ce, Y, and Sm doping on the thermoelectric properties of Bi2Te3 alloy, Prog. Nat. Sci-Mater. 23 (2013) 408–412, https://doi.org/10.1016/j.pnsc.2013.06.007.

[10] I. Malik, T. Srivastava, K.K. Surthi, C. Gayner, K.K. Kar, Enhanced thermoelectric performance of n–type Bi2Te3 alloyed with low cost and highly abundant sulfur, Mater. Chem. Phys. 255 (2020), https://doi.org/10.1016/j.matchemphys.2020.123598.

[11] Q.H. Jiang, J.Y. Yang, J.W. Xin, Z.W. Zhou, D. Zhang, H.X. Yan, Carriers concentration tailoring and phonon scattering from n–type zinc oxide (ZnO) nanoinclusion in p– and n–type bismuth telluride (Bi2Te3): Leading to ultra low thermal conductivity and excellent thermoelectric properties, J. Alloys Compd. 694 (2017) 864–868, https://doi.org/10.1016/j.jallcom.2016.10.076.

[12] J.U. Rahman, W.H. Nam, Y.J. Jung, J.H. Won, J.M. Oh, N. Van Du, G. Rahman, V. M. Garcia-Suarez, R. He, K. Nielsch, J.Y. Cho, W.S. Seo, J.W. Roh, S.I. Kim, S. Lee, K.H. Lee, H.S. Kim, W.H. Shin, Realizing high thermoelectric performance in n–type Se–free Bi2Te3 materials by spontaneous incorporation of FeTe2 nanoinclusions, Energy Environ. Sci. 7 (2024), https://doi.org/10.1002/eem2.12663.

[13] J.K. Chen, X.Y. Zhou, G.J. Snyder, C. Uher, N.F. Chen, Z.Y. Wen, J. Jin, H.L. Dong, P.F. Qiu, Y.F. Zhou, X. Shi, L.D. Chen, Direct tuning of electrical properties in nano–structured Bi2Se0.3Te2.7 by reversible electrochemical lithium reactions, Chem. Commun. 47 (2011) 12173–12175, https://doi.org/10.1039/c1cc15498b.

[14] C. Gayner, L.T. Menezes, Y. Natanzon, Y. Kauffmann, H. Kleinke, Y. Amouyal, Development of nanostructured Bi2Te3 with high thermoelectric performance by scalable synthesis and microstructure manipulations, ACS Appl. Mater. Interfaces 15 (2023) 13012–13024, https://doi.org/10.1021/acsami.2c21561.

[15] Q.X. Hu, W.D. Liu, L. Zhang, H. Gao, D.Z. Wang, T. Wu, X.L. Shi, M. Li, Q.F. Liu, Y. L. Yang, Z.G. Chen, Carrier separation boosts thermoelectric performance of flexible n–type Ag2Se–based films, Adv. Energy Mater. 14 (2024) 2401890, https://doi.org/10.1002/aenm.202401890.

[16] L.Q. Wang, J.Q. Li, C.X. Zhang, T. Ding, Y.C. Xie, Y. Li, F.S. Liu, W.Q. Ao, C. H. Zhang, Discovery of low–temperature GeTe–based thermoelectric alloys with high performance competing with Bi2Te3, J. Mater. Chem. A 8 (2020) 1660–1667, https://doi.org/10.1039/c9ta11901a.

[17] Z.H. Liu, N. Sato, W.H. Gao, K. Yubuta, N. Kawamoto, M. Mitome, K. Kurashima, Y. Owada, K. Nagase, C.H. Lee, J. Yi, K. Tsuchiya, T. Mori, Demonstration of ultrahigh thermoelectric efficiency of ∼7.3% in Mg3Sb2/MgAgSb module for low–temperature energy harvesting, Joule 5 (2021) 1196–1208, https://doi.org/10.1016/j.joule.2021.03.017.

[18] M. Thesberg, H. Kosina, N. Neophytou, On the effectiveness of the thermoelectric energy filtering mechanism in low–dimensional superlattices and nanocomposites, J. Appl. Phys. 120 (2016) 234302, https://doi.org/10.1063/1.4972192.

[19] Z. Liang, M.J. Boland, K. Butrouna, D.R. Strachan, K.R. Graham, Increased power factors of organic–inorganic nanocomposite thermoelectric materials and the role of energy filtering, J. Mater. Chem. A 5 (2017) 15891–15900, https://doi.org/10.1039/c7ta02307c.

[20] Y.C. Dou, X.Y. Qin, D. Li, L.L. Li, T.H. Zou, Q.Q. Wang, Enhanced thermopower and thermoelectric performance through energy filtering of carriers in (Bi2Te3)0.2 (Sb2Te3)0.8 bulk alloy embedded with amorphous SiO2 nanoparticles, J. Appl. Phys. 114 (2013) 044906, https://doi.org/10.1063/1.4817074.

[21] A.T. Serbesa, V. Pal, S.S. Legese, S. Mukherjee, S. Das, B. Kumar, C.G. Adamo, P. R. Sreeram, M. Paliwal, E.F. Olu, C.S. Tiwary, K. Chattopadhyay, Microstructure and thermoelectric properties of as–cast Ag2Te/AgBiTe2 and Ag2Te/Bi2Te3 two–phase alloys, J. Phys. Chem. Solids 190 (2024) 111995, https://doi.org/10.1016/j.jpcs.2024.111995.

[22] S.A. Yamini, R. Santos, R. Fortulan, A.A. Gazder, A. Malhotra, D. Vashaee, I. Serhiienko, T. Mori, Room–temperature thermoelectric performance of n–type multiphase pseudobinary Bi2Te3–Bi2S3 compounds: synergic effects of phonon scattering and energy filtering, ACS Appl. Mater. Interfaces 15 (2023) 19220–19229, https://doi.org/10.1021/acsami.3c01956.

[23] Y. Min, J.W. Roh, H. Yang, M. Park, S.I. Kim, S. Hwang, S.M. Lee, K.H. Lee, U. Jeong, Surfactant–free scalable synthesis of Bi2Te3 and Bi2Se3 nanoflakes and enhanced thermoelectric properties of their nanocomposites, Adv. Mater. 25 (2013) 1425–1429, https://doi.org/10.1002/adma.201203764.

[24] H. Hazama, Y. Masuoka, H. Yamamoto, H. Suto, Y. Kinoshita, M. Ishikiriyama, R. Asahi, Improvement of power factor of n–type Bi2Te3 by dispersed nanosized Ga2Te3 precipitates, J. Alloys Compd. 726 (2017) 578–586, https://doi.org/10.1016/j.jallcom.2017.07.272.

[25] C. Kim, J.Y. Baek, D.H. Lopez, D.H. Kim, H. Kim, Decoupling effect of electrical and thermal properties of Bi2Te3–polypyrrole hybrid material causing remarkable enhancement in thermoelectric performance, J. Ind. Eng. Chem. 71 (2019) 119–126, https://doi.org/10.1016/j.jiec.2018.11.013.

[26] C. Kim, J. Cho, T. Kim, D.H. Lopez, Interfacial effects in an inorganic/organic composite based on Bi2Te3 inducing decoupled transport properties and enhanced thermoelectric performance, J. Mater. Chem. A 10 (2022) 13780–13792, https://doi.org/10.1039/d2ta02334b.

[27] C. Kim, T. Kim, J. Cho, D.H. Lopez, Selective charge carrier transport and bipolar conduction in an inorganic/organic bulk phase composite: optimization for low temperature thermoelectric performance, ACS Appl. Mater. Interfaces 16 (2024) 5036–5049, https://doi.org/10.1021/acsami.3c11235.

[28] B. Ryu, Work function of bismuth telluride: First–principles approach, J. Korean Phys. Soc. 72 (2018) 122–128, https://doi.org/10.3938/jkps.72.122.

[29] D. Haneman, Photoelectric emission and work functions of InSb, GaAs, Bi2Te3 and germanium, J. Phys. Chem. Solids 11 (1959) 205–214, https://doi.org/10.1016/0022-3697(59)90215-X.

[30] Y. Zhang, H.L. Luo, H.H. Li, J.W. Wei, W.J. Cao, J. Jiang, W. Lu, X. Zhang, M.F. Liu, B. Zhang, A new strategy to simultaneously optimize Seebeck coefficient and electrical conductivity of PEDOT:PSS polymer via L–ascorbic acid, Synth. Met. 308 (2024) 117725, https://doi.org/10.1016/j.synthmet.2024.117725.

[31] T. Wu, X.L. Shi, Y.Y. Deng, Y.M. Liu, M. Zhu, W.D. Liu, M. Li, F. Yue, P. Huang, Z. G. Chen, Q.F. Liu, Incorporating graphene quantum dots boosts thermoelectric performance of PEDOT:PSS films, Chem. Eng. J. 506 (2025) 160219, https://doi.org/10.1016/j.cej.2025.160219.

[32] X. Fan, W.Y. Nie, S.H. Tsai, N.X. Wang, H.H. Huang, Y.J. Cheng, R.J. Wen, L.J. Ma, F. Yan, Y.G. Xia, PEDOT:PSS for flexible and stretchable electronics: modifications, strategies, and applications, Adv. Sci. 6 (2019) 1900813, https://doi.org/10.1002/advs.201900813.

[33] A. Soni, Y.Y. Zhao, L.G. Yu, M.K.K. Aik, M.S. Dresselhaus, Q.H. Xiong, Enhanced thermoelectric properties of solution grown Bi2Te3–xSex nanoplatelet composites, Nano Lett. 12 (2012) 1203–1209, https://doi.org/10.1021/nl2034859.

[34] J.O. Jenkins, R.W. Ure, J.A. Rayne, Elastic moduli and phonon properties of Bi2Te3, Phys. Rev. B 5 (1972) 3171–3184, https://doi.org/10.1103/PhysRevB.5.3171.

[35] X. Guo, J. Jian, L. Lin, H. Zhu, S. Zhu, O2 plasma–functionalized SWCNTs and PEDOT/PSS composite film assembled by dielectrophoresis for ultrasensitive trimethylamine gas sensor, Analyst 138 (2013) 5265–5273, https://doi.org/10.1039/c3an36690a.

[36] G. Greczynski, T. Kugler, W.R. Salaneck, Characterization of the PEDOT–PSS system by means of X–ray and ultraviolet photoelectron spectroscopy, Thin Solid Films 354 (1999) 129–135, https://doi.org/10.1016/s0040-6090(99)00422-8.

[37] G.J. Snyder, A.H. Snyder, M. Wood, R. Gurunathan, B.H. Snyder, C. Niu, Weighted mobility, Adv. Mater. 32 (2020) 2001537, https://doi.org/10.1002/adma.202001537.

[38] B. Qin, W. He, L.D. Zhao, Estimation of the potential performance in p–type SnSe crystals through evaluating weighted mobility and effective mass, J. Materiom. 6 (2020) 671–676, https://doi.org/10.1016/j.jmat.2020.06.003.

[39] Q. Ren, C. Fu, Q. Qiu, S. Dai, Z. Liu, T. Masuda, S. Asai, M. Hagihala, S. Lee, S. Torri, T. Kamiyama, L. He, X. Tong, C. Felser, D.J. Singh, T. Zhu, J. Yang, J. Ma, Establishing the carrier scattering phase diagram for ZrNiSn–based half–Heusler thermoelectric materials, Nat. Commun. 11 (2020) 3142, https://doi.org/10.1038/s41467-020-16913-2.

[40] H.S. Kim, Z.M. Gibbs, Y.L. Tang, H. Wang, G.J. Snyder, Characterization of Lorenz number with Seebeck coefficient measurement, APL Mater. 3 (2015) 041506, https://doi.org/10.1063/1.4908244.

[41] F. Hao, P.F. Qiu, Y.S. Tang, S.Q. Bai, T. Xing, H.S. Chu, Q.H. Zhang, P. Lu, T. S. Zhang, D.D. Ren, J.K. Chen, X. Shi, L.D. Chen, High efficiency Bi2Te3–based materials and devices for thermoelectric power generation between 100 and 300 °C, Energy Environ. Sci. 9 (2016) 3120–3127, https://doi.org/10.1039/c6ee02017h.

[42] K. Ghosh, A. Kusiak, J.L. Battaglia, Phonon hydrodynamics in crystalline GeTe at low temperature, Phys. Rev. B 102 (2020) 094311, https://doi.org/10.1103/PhysRevB.102.094311.

[43] G. Wu, Q. Zhang, X.J. Tan, Y.T. Fu, Z. Guo, Z.W. Zhang, Q.Q. Sun, Y. Liu, H.L. Shi, J.S. Li, J.G. Noudem, J.H. Wu, G.Q. Liu, P. Sun, H.Y. Hu, J. Jiang, Bi2Te3–based thermoelectric modules for efficient and reliable low–grade heat recovery, Adv. Mater. 36 (2024) 2400285, https://doi.org/10.1002/adma.202400285.

[44] Y. Saberi, S.A. Sajjadi, A comprehensive review on the effects of doping process on the thermoelectric properties of Bi2Te3 based alloys, J. Alloys Compd. 904 (2022) 163918, https://doi.org/10.1016/j.jallcom.2022.163918.

[45] B. Qiu, H. Bao, G. Zhang, Y. Wu, X. Ruan, Molecular dynamics simulations of lattice thermal conductivity and spectral phonon mean free path of PbTe: bulk and nanostructures, Comput. Mater. Sci. 53 (2012) 278–285, https://doi.org/10.1016/j.commatsci.2011.08.016.

[46] J.H. Bahk, A. Shakouri, Minority carrier blocking to enhance the thermoelectric figure of merit in narrow–band–gap semiconductors, Phys. Rev. B 93 (2016) 165209, https://doi.org/10.1103/physrevb.93.165209.

[47] Z.C. Huang, K. Hayashi, W. Saito, H.Z. Li, J. Pei, J.F. Dong, T. Chiba, X. Nan, B. P. Zhang, J.F. Li, Y. Miyazaki, Dislocation introduction via domain engineering in Mg2Sn single crystal to improve its thermoelectric properties, Small Methods 9 (2025) 2500385, https://doi.org/10.1002/smtd.202500385.

[48] L. Hu, H. Wu, T. Zhu, C. Fu, J. He, P. Ying, X. Zhao, Tuning multiscale microstructures to enhance thermoelectric performance of n–type bismuth–telluride–based solid solutions, Adv. Energy Mater. 5 (2015) 1500411, https://doi.org/10.1002/aenm.201500411.

[49] H. Lee, T. Kim, S.C. Son, J. Kim, D. Kim, J. Lee, I. Chung, Unique microstructures and high thermoelectric performance in n–type Bi2Te2.7Se0.3 by the dual incorporation of Cu and Y, Mater. Today Phys. 31 (2023) 100986, https://doi.org/10.1016/j.mtphys.2023.100986.

[50] B. Zhu, Z.-Y. Huang, X.-Y. Wang, Y. Yu, L. Yang, N. Gao, Z.-G. Chen, F.-Q. Zu, Attaining ultrahigh thermoelectric performance of direction–solidified bulk n–type Bi2Te2.4Se0.6 via its liquid state treatment, Nano Energy 42 (2017) 8–16, https://doi.org/10.1016/j.nanoen.2017.10.034.

[51] Q. Hu, J. Guo, H. Zuo, H. Chen, Enhanced thermoelectric properties of n–type Bi2Te2.7Se0.3 materials by TiO2 ceramic nanoparticle dispersion–induced energy filtering effect, Ceram. Int. 49 (2023) 32144–32152, https://doi.org/10.1016/j.ceramint.2023.07.183.

[52] B. Zhu, X. Liu, Q. Wang, Y. Qiu, Z. Shu, Z. Guo, Y. Tong, J. Cui, M. Gu, J. He, Realizing record high performance in n–type Bi2Te3–based thermoelectric materials, Energy Environ. Sci. 13 (2020) 2106–2114, https://doi.org/10.1039/d0ee01349h.